Effects of magnetic ordering on the anisotropy and temperature dependence of the optical conductivity in $LaMnO_3$: A tight-binding approach

K. H. Ahn* and A. J. Millis
Department of Physics and Astronomy, Rutgers University, Piscataway, New Jersey 08854
(Received 14 January 1999; revised manuscript received 29 November 1999)

A tight-binding parametrization of the band structure, along with a mean-field treatment of the Hund, electron-electron, and electron-lattice couplings, is used to obtain the full optical conductivity tensor of $LaMnO_3$ as a function of temperature. We predict striking changes with temperature in the functional form and magnitude of the optical absorption. Comparison of our results with existing data makes it possible to determine the electron-lattice and electron-electron couplings. The effective ''Hubbard U'' is found to be ≈ 1.6 eV, rather less than the full bandwidth ≈ 3.6 eV, putting the material in the weak-intermediate coupling regime.

I. INTRODUCTION

In this paper we present calculations of the temperature-dependent optical conductivity of $LaMnO_3$. Our work has two motivations. One is to help clarify the physics of an important class of materials. $LaMnO_3$ is the ''parent compound'' of the ''colossal'' magnetoresistance compounds, which are currently the subject of intense theoretical, experimental, and applied interest.[1] Our results suggest that the optical conductivity of the parent compound exhibits characteristic structures, frequency scales, and temperature dependences, from which the important interactions and energy scales may be deduced, and the consistency of the theory and data may be verified. In particular, we show how estimates of the Hund's coupling and the effective Coulomb repulsion may be obtained. The values of both of these parameters have been the subject of controversy in literature.[2–4]

Our second motivation concerns the theory of optical conductivity of ''correlated electron'' systems. Most theoretical studies of optical conductivity of correlated electron materials (including the one presented here) make a fundamental approximation: The underlying band structure is represented by a tight-binding model and the optical matrix elements are computed via the ''Peierls phase'' method. The approximation is made because correlation effects may be studied much more conveniently and in much more detail in a nearest-neighbor tight-binding model (such as the Hubbard model) than in a full band-structure calculation. However, few detailed quantitative comparisons between the results found from simple tight-binding-based calculations and the results from experimental data or the results found via other theoretical techniques have appeared, and therefore the limitations of the simple tight-binding-plus-interactions approach are not clear. The work presented here is a step towards such a comparison. In addition to relating the results of our calculations to available data and to other calculations, we introduce a general framework, emphasizing robust features of the conductivity, in terms of which comparisons should be made. We also argue that particular features of the $LaMnO_3$ family of materials (especially the ''tunable'' kinetic energy explained in more detail below) make them ideal materials on which to test a general theory of conductivity of correlated materials.

The paper is organized as follows. Section II introduces the material, the Hamiltonian, the approximation, and the formalism used to compute the conductivity. Section III presents our results. Section IV compares our results to available data. Section V discusses the theoretical status of our results, considers the magnitude of errors introduced by the approximations we have made, and notes a troubling discrepancy between our results and those obtained by a different method.[5,6] Section VI is a conclusion.

II. MATERIAL, MODEL, AND METHODS OF CALCULATION

A. Overview

$LaMnO_3$ exists in a distorted form of the ABO_3 perovskite structure. The important ions in $LaMnO_3$ are the Mn ions, with nominal valence Mn^{3+}, corresponding to four 3d electrons. The actual states are linear combinations mainly of Mn e_g orbitals and O $2p$ orbitals, but this will not play any role in our subsequent considerations and we will hereafter refer to the states as e_g levels. A strong Hund's coupling makes all four electrons' spins parallel with each other. An approximately cubic crystal field due to the oxygen octahedron around the Mn ion splits the Mn 3d levels into t_{2g} (xy,yz,zx) and e_g $(x^2-y^2, 3z^2-r^2)$ levels. Three electrons occupy the t_{2g} core levels, and one electron occupies a linear combination of the two e_g levels. In the ideal perovskite structure the two e_g levels are degenerate, but in $LaMnO_3$ below $T=800$ K a cooperative Jahn-Teller (JT) distortion occurs,[7] which essentially preserves the unit-cell volume and bond angle, but makes some Mn-O bonds shorter than average and some longer. The structural change consists of two components: a uniform Q_3-type tetragonal distortion, which shortens one lattice constant (along z direction) and lengthens the other two (along x and y directions), and a Q_2-type $(\pi,\pi,0)$ staggered distortion, which introduces alternating Mn-O bond lengths in the xy plane. In addition to these distortions, small bucklings of oxygen octahedrons exist. However, we believe these bucklings have little effect on optical conductivity, as we explain in more detail in the next section. As T is decreased through 140 K, a magnetic transition to an A-type antiferromagnet, with ferromagnetic ordering in the xy plane and antiferromagnetic ordering along the z direction, occurs. This magnetic ordering produces a marked temperature-dependent anisotropy.

B. Model Hamiltonian

1. Choice of orbitals

In this paper, we focus on low-energy excitations ($\lesssim 4$ eV) that contribute to optical conductivity. According to band-theory calculations,[8–10] the Mn e_g-symmetric d levels are near the Fermi energy and well separated from other bands except for those derived from the Mn t_{2g} orbitals. We believe that the t_{2g} band is not important for the optical conductivity we study. Our reasons are as follows: First, the band theory and the magnetic measurements agree that all t_{2g} electrons have parallel spins and form a filled shell that is expected to be electrically inert. Indeed, the t_{2g} band has a narrow bandwidth (about one-third of the e_g band), implying a small hopping amplitude. The band structure also shows that the t_{2g} to t_{2g} transition requires energy more than about 3 eV, and the Coulomb interaction will increase this. Therefore, the t_{2g} to t_{2g} excitations require higher energies and have a smaller optical spectral weight than the e_g to e_g excitations. Second, the mixing between the e_g and t_{2g} levels is small. In a simple nearest-neighbor tight-binding model for a perovskite structure with 180° Mn-O-Mn bonds, due to the symmetry about the Mn-O-Mn axis, the Mn t_{2g} orbitals hybridize only with O 2p π orbitals, whereas the Mn e_g orbitals hybridize only with O 2p σ orbitals, which forbids the e_g and t_{2g} mixing. Even after further neighbor hoppings and bond bucklings are included, the admixture between e_g and t_{2g} will be very weak compared to the e_g and e_g mixing. The band structure for the system that does not have buckling of oxygen octahedrons was calculated in Ref. 9, which shows that the e_g and t_{2g} bands cross with a tiny gap less than 0.02 eV (0.6% of the total e_g bandwidth). The buckling of the oxygen octahedrons increases the mixing as shown between Γ and T points in Fig. 2(a) in Ref. 8. The $e_g^1 \uparrow$ band and the $t_{2g} \uparrow$ band mix and open a gap ≈ 0.26 eV (about 7% of the $e_g \uparrow$ bandwidth), which is still small. Therefore, we believe that the low-energy excitations can be well described by the Mn e_g band only.

2. Model Hamiltonian for T=0 K

We find that the band structure appropriate to the ideal cubic ABO_3 perovskite structure may be well represented by the following tight-binding model:

$$H_{\mathrm{KE}}+H_{\mu}=-\frac{1}{2}\sum_{\vec{i},\vec{\delta},a,b,\alpha} t_{\vec{\delta}}^{ab} d_{\vec{i}a\alpha}^{\dagger} d_{\vec{i}+\vec{\delta}b\alpha}+\mathrm{H.c.} \\ -\mu\sum_{\vec{i},a,\alpha} d_{\vec{i}a\alpha}^{\dagger} d_{\vec{i}a\alpha}. \tag{1}$$

Here $\vec{i}$ represents the coordinates of the Mn sites, which in the ideal structure are arranged in a simple cubic lattice, a and b represent the two degenerate Mn e_g orbitals on a site, δ $(=\pm x,y,z)$ labels the nearest neighbors of a Mn site, α denotes the spin state, and $t_{\vec{\delta}}^{ab}$ is the hopping amplitude between orbital a on site $\vec{i}$ and b on site $\vec{i}+\vec{\delta}$. We choose $|\psi_1\rangle=|3z^2-r^2\rangle$ and $|\psi_2\rangle=|x^2-y^2\rangle$ as the two linearly independent e_g orbitals on a site. The hopping matrix $t_{\vec{\delta}}^{ab}$ has a special form: For hopping along the z direction, it connects only the two $|3z^2-r^2\rangle$ states, thus

$$t_z=t_{-z}=t_0\begin{pmatrix}1 & 0\\ 0 & 0\end{pmatrix}. \tag{2}$$

The hopping matrices in the other bond directions are obtained by the appropriate rotations and are

$$t_x=t_{-x}=t_0\begin{pmatrix}1/4 & -\sqrt{3}/4\\ -\sqrt{3}/4 & 3/4\end{pmatrix}, \tag{3}$$

$$t_y=t_{-y}=t_0\begin{pmatrix}1/4 & \sqrt{3}/4\\ \sqrt{3}/4 & 3/4\end{pmatrix}. \tag{4}$$

There is substantial high-energy photoemission evidence for the strong on-site Coulomb interactions ($U_{\mathrm{bare}}\approx 8$ eV) in the manganites, which places them in the class of ''charge-transfer'' materials. The relevance of the band-theory calculation may therefore be questioned. We argue, however, that the effects of the interactions at the low ($\hbar\omega<4$ eV) energies of interest may be determined by comparing the predictions of the band-theory calculation to data; the results we present will allow this comparison to be made.

The high-T_c superconductors provide an instructive example. These are also charge-transfer insulators with a very large high-energy on-site repulsion U_{high} (Refs. 11 and 12). The low-energy excitations are complicated objects called the Zhang-Rice singlets, but it has been established that the effective interaction relevant to the low-energy theory is much less than U_{high}, and that band theory (albeit with a renormalized hopping) describes the electron dispersion well. We therefore suggest that band theory is an appropriate starting point in the manganite case as well.

We now turn to the electron-lattice coupling. Below 800 K, $LaMnO_3$ exists in a distorted form of the ABO_3 perovskite structure. The important distortion is a Jahn-Teller distortion, which lifts the degeneracy of the e_g levels on a site. To represent this, we define $u_{\vec{i}}^{\eta}$ $(\eta=x,y,z)$ as the $\hat{\eta}$ direction displacement of an oxygen ion located between Mn ions at $\vec{i}$ and $\vec{i}+\hat{\eta}$, and we define $v_{\vec{i}}^{\eta}=u_{\vec{i}}^{\eta}-u_{\vec{i}-\hat{\eta}}^{\eta}$. The Jahn-Teller distortion term may then be written as

$$H_{\mathrm{JT}}=-\lambda\sum_{\vec{i}\alpha}\begin{pmatrix}d_{1,\vec{i},\alpha}^{\dagger}\\ d_{2,\vec{i},\alpha}^{\dagger}\end{pmatrix}^{T}\begin{pmatrix}v_{\vec{i}}^{z}-\frac{1}{2}(v_{\vec{i}}^{x}+v_{\vec{i}}^{y}) & \frac{\sqrt{3}}{2}(v_{\vec{i}}^{x}-v_{\vec{i}}^{y})\\ \frac{\sqrt{3}}{2}(v_{\vec{i}}^{x}-v_{\vec{i}}^{y}) & -v_{\vec{i}}^{z}+\frac{1}{2}(v_{\vec{i}}^{x}+v_{\vec{i}}^{y})\end{pmatrix}\begin{pmatrix}d_{1,\vec{i},\alpha}\\ d_{2,\vec{i},\alpha}\end{pmatrix}, \tag{5}$$

which defines the Jahn-Teller coupling constant λ in our model. The experimentally observed distortion has two components: a Q_2-type staggered distortion with wave vector $(\pi,\pi,0)$, and a Q_3-type uniform distortion. This distortion leads to a Jahn-Teller term of the form

$$H_{\mathrm{JT}}=-\lambda\sum_{\vec{i},\alpha}\begin{pmatrix} d^{\dagger}_{1,\vec{i},\alpha} \\ d^{\dagger}_{2,\vec{i},\alpha}\end{pmatrix}^{T}\begin{pmatrix} -\overline{v} & (-1)^{i_x+i_y}\overline{w} \\ (-1)^{i_x+i_y}\overline{w} & \overline{v}\end{pmatrix}\begin{pmatrix} d_{1,\vec{i},\alpha} \\ d_{2,\vec{i},\alpha}\end{pmatrix}, \tag{6}$$

where $\overline{w}$ and $\overline{v}$ are the amplitudes of the staggered (Q_2) and the uniform (Q_3) distortions, respectively.

We next consider the Hund's coupling. This leads to a term

$$H_{\mathrm{Hund}}=\sum_{\vec{i},a,\alpha} J_{\mathrm{H}}\vec{S}^{t}_{\mathrm{c}}\cdot d^{\dagger}_{\vec{i},a,\alpha}\vec{\sigma}_{\alpha\beta}d_{\vec{i},a,\beta}, \tag{7}$$

where $\vec{S}^{t}_{\mathrm{c}}$ represents the t_{2g} core spin and $\vec{\sigma}$ the Pauli matrix. At $T=0$ K, the magnetic structure is of a $(0,0,\pi)$ antiferromagnet, which leads to

$$H_{\mathrm{Hund}}=J_{\mathrm{H}}S_{\mathrm{c}}\sum_{\vec{i},a}\{[1-(-1)^{i_z}]d^{\dagger}_{\vec{i},a,\uparrow}d_{\vec{i},a,\uparrow} +[1+(-1)^{i_z}]d^{\dagger}_{\vec{i},a,\downarrow}d_{\vec{i},a,\downarrow}\}. \tag{8}$$

We now add an on-site Hubbard-type Coulomb repulsion to our Hamiltonian. Because we have two orbital and two spin states on each site, we have in principle six different Coulomb repulsion terms, which may be generally written ($\hat{n}$ is the density operator)

$$H_{\mathrm{Coulomb}}=\sum_{\vec{i}}\sum_{(\alpha,a)\neq(\beta,b)}U_{(\alpha,a),(\beta,b)}\hat{n}_{\vec{i},\alpha,a}\hat{n}_{\vec{i}\beta,b}. \tag{9}$$

The total Hamiltonian is the sum of the terms considered so far:

$$H^{0K}_{\mathrm{tot}}=H_{\mathrm{KE}}+H_{\mu}+H_{\mathrm{JT}}+H_{\mathrm{Hund}}+H_{\mathrm{Coulomb}}. \tag{10}$$

We study the band structure of $H^{0K}_{\mathrm{nonint}}=H_{\mathrm{KE}}+H_{\mu}+H_{\mathrm{JT}}+H_{\mathrm{Hund}}$, the noninteracting part of the Hamiltonian, at $T=0$ K. By diagonalizing the k space representation given in Appendix A, we find the band structure. At $T=0$ K, the unit cell is doubled twice, once by spin and once by orbital ordering. We have two orbital states for each of the two spin states, and four Mn sites per unit cell. Due to the symmetry between the two spin states, we will have twofold degeneracy for each level. Therefore, we have eight separate bands. The ground state is obtained by filling the energy levels below the chemical potential μ, which is determined to give the correct number of electrons per unit cell. We denote the energy levels by $E_j(\vec{k})$ with $j=1,2,\ldots,8$ in the order of the increasing energy. Our tight-binding band structure is shown in Fig. 1 for the parameters which provide the best fit to the published band calculations.[9] Crudely speaking, the bands fall into four pairs, which may be understood by setting $t_0=0$ [as occurs at $(\pi/2,\pi/2,\pi/2)$]. In this case we have four separate energy levels on each site, which are $E_{1,2}=-\lambda\sqrt{\overline{v}^2+\overline{w}^2}$, $E_{3,4}=\lambda\sqrt{\overline{v}^2+\overline{w}^2}$, $E_{5,6}=2J_{\mathrm{H}}S_{\mathrm{c}}-\lambda\sqrt{\overline{v}^2+\overline{w}^2}$, and $E_{7,8}=2J_{\mathrm{H}}S_{\mathrm{c}}+\lambda\sqrt{\overline{v}^2+\overline{w}^2}$. In the $(0,0,\pi)$ antiferromagnetic structure at $T=0$ K, the Hund's coupling suppresses the z-directional hopping; the bands thus become more two-dimensional as $J_{\mathrm{H}}S_{\mathrm{c}}$ increases.

3. Model Hamiltonian for $T_N \ll T \ll 800$ K

In this subsection, we indicate the modifications needed to describe $LaMnO_3$ in the paramagnetic state, in particular at around $T=300$ K$\gg T_{\mathrm{N}}$. For $T\gg T_{\mathrm{N}}$, it is reasonable to assume that the core spins are completely disordered. However, because room temperature is much lower than the structural transition temperature 800 K, we may neglect lattice fluctuations and assume a static JT distortion with magnitude similar to the $T=0$ K one.

To describe the system at $T_{\mathrm{N}}\ll T\ll 800$ K, we use a spatially varying spin basis in which $\Uparrow$ on site $\vec{i}$ indicates the e_g spin parallel to the core spin on site $\vec{i}$ and $\Downarrow$ indicates the e_g spin antiparallel to the core spin. In this basis, the Hund's coupling energy corresponds to the shift of the spin-down bands:

$$H_{\mathrm{Hund}}=2J_{\mathrm{H}}S_{\mathrm{c}}\sum_{\vec{i},a}d^{\dagger}_{\vec{i},a,\Downarrow}d_{\vec{i},a,\Downarrow}. \tag{11}$$

The hopping amplitudes are modified by spin overlap factors. To write this, we define the angle between the core spin directions on site $\vec{i}$ and on site $\vec{i}+\vec{\delta}$ as $\theta_{\vec{i},\vec{i}+\vec{\delta}}$, so that the kinetic energy is given by

$$H_{\mathrm{KE}}=-\frac{1}{2}\sum_{\vec{i},\vec{\delta},a,b}t^{ab}_{\vec{\delta}}\left[\cos\left(\frac{\theta_{\vec{i},\vec{i}+\vec{\delta}}}{2}\right)d^{\dagger}_{\vec{i}a\Uparrow}d_{\vec{i}+\vec{\delta}b\Uparrow}+\cos\left(\frac{\theta_{\vec{i},\vec{i}+\vec{\delta}}}{2}\right)d^{\dagger}_{\vec{i}a\Downarrow}d_{\vec{i}+\vec{\delta}b\Downarrow} +\sin\left(\frac{\theta_{\vec{i},\vec{i}+\vec{\delta}}}{2}\right)d^{\dagger}_{\vec{i}a\Uparrow}d_{\vec{i}+\vec{\delta}b\Downarrow}+\sin\left(\frac{\theta_{\vec{i},\vec{i}+\vec{\delta}}}{2}\right)d^{\dagger}_{\vec{i}a\Downarrow}d_{\vec{i}+\vec{\delta}b\Uparrow}+\mathrm{H.c.}\right]. \tag{12}$$

At $T\gg T_{\mathrm{N}}$, $\theta_{\vec{i},\vec{i}+\vec{\delta}}$ will be completely random. Therefore, we argue that it is appropriate to average the Hamiltonian by setting $\langle\cos(\theta_{\vec{i},\vec{i}+\vec{\delta}}/2)\rangle=\langle\sin(\theta_{\vec{i},\vec{i}+\vec{\delta}}/2)\rangle=2/3$, which gives the following effective kinetic energy term

$$H^{300\ \mathrm{K,eff}}_{\mathrm{KE}}=-\frac{1}{3}\sum_{\vec{i},\vec{\delta},a,b}t^{ab}_{\vec{\delta}}[d^{\dagger}_{\vec{i}a\Uparrow}d_{\vec{i}+\vec{\delta}b\Uparrow}+d^{\dagger}_{\vec{i}a\Downarrow}d_{\vec{i}+\vec{\delta}b\Downarrow}+d^{\dagger}_{\vec{i}a\Uparrow}d_{\vec{i}+\vec{\delta}b\Downarrow}+d^{\dagger}_{\vec{i}a\Downarrow}d_{\vec{i}+\vec{\delta}b\Uparrow}+\mathrm{H.c.}]. \tag{13}$$

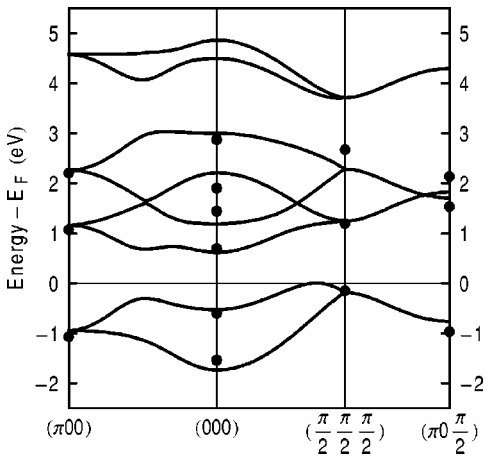

FIG. 1. Fitted e_g band structure of $LaMnO_3$: $t_0=0.622$ eV, $2J_HS_c=2.47$ eV, $\lambda=1.38$ eV/Å, and $\mu=0.4$ eV. $(\pi,0,0)$, $(0,0,0)$, $(\pi/2,\pi/2,\pi/2)$, and $(\pi,0,\pi/2)$ points correspond to M, Γ, R, and A points in Ref. 9, respectively. The dots represent the energy levels of the LDA calculation in Ref. 9, with which we fitted our model.

H_μ, $H_{\rm JT}$, and $H_{\rm Coulomb}$ do not change their forms with the change of the spin basis. The $\vec{k}$ space representation of $H_{\rm nonint}^{300\ {\rm K}}=H_{\rm KE}^{300\ {\rm K,eff}}+H_\mu+H_{\rm JT}+H_{\rm Hund}$ is shown in Appendix B.

C. Hartree-Fock approximation of the Coulomb interaction

We take the Hartree-Fock approximation of the Coulomb interaction, which we believe is reasonably accurate for the simple quantities (peak position and spectral weight) important for our analysis. Corrections to the Hartree-Fock approximation are due to quantum fluctuations. We have compared the Hartree-Fock approximation to the exact results for the case of the strongest fluctuations, namely the one-dimensional Hubbard model, studied by Stafford.[13] We use the Hartree-Fock approximation for one electron per site case and obtain the total kinetic energy, which is proportional to the total spectral weight. The results are shown in Table I, in which we also show the exact results in Ref. 13, and the high-U limit approximation, $4t^2/U$. It shows that the Hartree-Fock approximation is in agreement with the exact results within 30%. We believe that in the case of present interest, the combination of three dimensionality, the large core spins, and the localization due to the electron-phonon interaction renders the Hartree-Fock approximation sufficiently accurate.

In this approximation, one of the two density operators is replaced by its expectation value, which is determined self-consistently. The approximation explicitly breaks symmetry in spin and orbital space, so the issue of basis choice arises. We choose the orbital basis picked out by the observed lattice distortion and the spin basis picked out by the magnetic ordering. We refer to the higher- and the lower-lying orbital states as $+$ and $-$, respectively, and the spin states by $\Uparrow$ and $\Downarrow$ as defined in the previous section. The Hartree-Fock Hamiltonian may then be written as

$$H_{\rm Coulomb}^{\rm HF}=\sum_{\vec{i}}\ U_{\Uparrow+}d_{\vec{i}\Uparrow+}^{\dagger}d_{\vec{i}\Uparrow+}+U_{\Uparrow-}d_{\vec{i}\Uparrow-}^{\dagger}d_{\vec{i}\Uparrow-}+U_{\Downarrow+}d_{\vec{i}\Downarrow+}^{\dagger}d_{\vec{i}\Downarrow+}+U_{\Downarrow-}d_{\vec{i}\Downarrow-}^{\dagger}d_{\vec{i}\Downarrow-}, \quad (14)$$

where $U_{\Uparrow,+}=U_{\Uparrow\Uparrow+-}\langle\hat{n}_{\Uparrow-}\rangle+U_{\Uparrow\Downarrow++}\langle\hat{n}_{\Downarrow+}\rangle+U_{\Uparrow\Downarrow+-}\langle\hat{n}_{\Downarrow-}\rangle$, etc.

This equation may be reorganized into a term proportional to the total e_g density operator, which renormalizes the chemical potential and is of no interest, a term that couples to the total e_g spin operator and changes the Hund's coupling, and terms that renormalize the local Jahn-Teller splitting in a manner that differs for electrons locally parallel and antiparallel to the core spins. Therefore, $H_{\rm JT}+H_{\rm Hund}+H_{\rm Coulomb}^{\rm HF}$ can be cast into the following form:

$$H_{\rm JT}+H_{\rm Hund}+H_{\rm Coulomb}^{\rm HF}=\sum_i\ \lambda'_{\Uparrow}\sqrt{\overline{v^2}+\overline{w^2}}(\hat{n}_{\vec{i}\Uparrow+}-\hat{n}_{\vec{i}\Uparrow-})+\lambda'_{\Downarrow}\sqrt{\overline{v^2}+\overline{w^2}}(\hat{n}_{\vec{i}\Downarrow+}-\hat{n}_{\vec{i}\Downarrow-})+2J'_{\rm H}S_{\rm c}(\hat{n}_{\vec{i}\Downarrow+}+\hat{n}_{\vec{i}\Downarrow-}), \quad (15)$$

where

$$\lambda'_{\Uparrow}=\lambda+\frac{U_{\Uparrow+}-U_{\Uparrow-}}{2\sqrt{\overline{v^2}+\overline{w^2}}}, \quad (16)$$

$$\lambda'_{\Downarrow}=\lambda+\frac{U_{\Downarrow+}-U_{\Downarrow-}}{2\sqrt{\overline{v^2}+\overline{w^2}}}, \quad (17)$$

$$2J'_{\rm H}S_{\rm c}=2J_{\rm H}S_{\rm c}+\frac{1}{2}(U_{\Downarrow+}+U_{\Downarrow-}-U_{\Uparrow+}-U_{\Uparrow-}). \quad (18)$$

We transform the above Hamiltonian into $|\psi_1\rangle=|3z^2-r^2\rangle$ and $|\psi_2\rangle=|x^2-y^2\rangle$ orbital basis, in which the hopping matrices are defined. The total Hartree-Fock Hamiltonians at $T=0$ K and 300 K are

$$H_{\rm tot}^{0\ {\rm K,HF}}=H_{\rm KE}+H_\mu+H_{\rm JT}+H_{\rm Hund}+H_{\rm Coulomb}^{\rm HF}, \quad (19)$$

$$H_{\rm tot}^{300\ {\rm K,HF}}=H_{\rm KE}^{300\ {\rm K,eff}}+H_\mu+H_{\rm JT}+H_{\rm Hund}+H_{\rm Coulomb}^{\rm HF}. \quad (20)$$

By representing the total Hartree-Fock Hamiltonian in k space, we obtain the results in Appendix C, in which we also presented the expressions of the number operators.

TABLE I. Total spectral weights represented in terms of kinetic energies for the one-dimensional Hubbard model with $t=1$ and $n=1$.

U	Exact kinetic energy from Ref. 13	Kinetic energy in Hartree-Fock approximation	Large-U limit, $4t^2/U$
0	1.27	1.27	Not applicable
4	0.97	0.77	1
8	0.62	0.46	0.5
∞	0	0	0

D. Optical conductivity

1. At $T=0$ K

Optical conductivity per volume, σ, is obtained using the standard linear-response theory explained in detail in Ref. 14 and used in Ref. 15. The electromagnetic field couples to the electrons via the Peierls phase factor $t_\delta \rightarrow t_\delta \exp(ie\vec{A}\cdot\vec{\delta}a_0/\hbar)$. By expanding $\langle \vec{J} \rangle = \langle \delta H/\delta \vec{A} \rangle$ to linear order in $\vec{A}$, we find

$$\sigma_{\eta\nu} = \sigma^d_{\eta\nu} + \sigma^p_{\eta\nu}, \tag{21}$$

$$\sigma^d_{\eta\nu} = -\frac{1}{i\omega}\left(\frac{ea_0}{\hbar}\right)^2 \delta_{\eta\nu} K_{\eta\eta} \frac{1}{a_0^3}, \tag{22}$$

$$\sigma^p_{\eta\nu} = -\frac{1}{i\omega N_{Mn} a_0^3} \sum_n \frac{\langle 0|J^\dagger_{p\eta}|n\rangle\langle n|J_{p\nu}|0\rangle}{\hbar\omega - (E_n - E_0) + i\epsilon}, \tag{23}$$

where

$$K_{\eta\eta} = \frac{1}{N_{Mn}} \langle 0| \frac{1}{2} \sum_{\vec{i},\vec{\delta}=\pm\hat{\eta},a,b,\alpha} t^{ab}_{\vec{\delta}} (d^\dagger_{\vec{i}a\alpha} d_{\vec{i}+\vec{\delta}b\alpha} + \text{H.c.}) |0\rangle, \tag{24}$$

$$\hat{\vec{J}}_p = -\frac{iea_0}{2\hbar} \sum_{\vec{i},\vec{\delta},a,b,\alpha} t^{ab}_{\vec{\delta}} \vec{\delta} (d^\dagger_{\vec{i}a\alpha} d_{\vec{i}+\vec{\delta}b\alpha} - \text{H.c.}), \tag{25}$$

ϵ is an infinitesimal introduced to make the expression well defined, and η, $\nu = x,y,z$. $K_{\eta\eta}$ is the kinetic energy along η $(=x,y,z)$ direction. a_0 is the distance between the Mn ions. By taking the large-ω limit and using the Kramers-Kronig relation, we obtain the following sum rule:

$$K_{\eta\eta} = \frac{\hbar^2 a_0}{e^2} \frac{2}{\pi} \int_0^\infty d\omega \, \text{Re}[\sigma_{\eta\eta}(\omega)]. \tag{26}$$

We have evaluated K and σ using the Hamiltonians and approximations listed above. At $T=0$ K, we find

$$K_{\eta\eta} = \frac{2}{(2\pi)^3} \int_R d\vec{k} \sum_{E_j(\vec{k})<\mu} 2\cos k_\eta B_\eta(\vec{k})_{jj} \tag{27}$$

and

$$(\sigma^p)_{\eta\eta} = -\frac{2}{i\omega a_0^3} \frac{1}{(2\pi)^3} \int_R d\vec{k} \sum_{E_j(\vec{k})<\mu, E_{j'}(\vec{k})>\mu} \frac{|(ea_0/\hbar) 2\sin k_\eta B_\eta(\vec{k})_{jj'}|^2}{\hbar\omega - E_{j'}(\vec{k}) + E_j(\vec{k}) + i\epsilon}, \tag{28}$$

where $B_\eta(\vec{k})$ is a matrix related to the current operator. Explicit expressions of $B_\eta(\vec{k})$ for $H^{0\ \text{K}}_{\text{nonint}}$ and $H^{0\ \text{K,HF}}_{\text{tot}}$ are given in Appendices A and C, respectively. R is the first Brillouin zone of the band structure of the fully ordered state. j and j' are the band indices. The factor of 2 is from the spin degeneracy. Therefore, the real part of σ at $T=0$ K is

$$\text{Re}[\sigma_{\eta\eta}] = \frac{2}{\omega a_0^3} \frac{1}{(2\pi)^3} \int_R d\vec{k} \sum_{E_j(\vec{k})<\mu, E_{j'}(\vec{k})>\mu} \left| \frac{ea_0}{\hbar} 2\sin k_\eta B_\eta(\vec{k})_{jj'} \right|^2 \frac{\epsilon}{[\hbar\omega - E_{j'}(\vec{k}) + E_j(\vec{k})]^2 + \epsilon^2}. \tag{29}$$

2. At $T_N \ll T \ll 800$ K

To compute the optical conductivity in the paramagnetic state, we use the effective Hamiltonian for $T=300$ K, and use the same method as the $T=0$ K case. Because at $T \gg T_N$, the core spin directions are fluctuating in time and space, the energy levels are broadened. To incorporate this physics, we introduce a phenomenological broadening parameter Γ of each energy level, leading to the following expression of the optical conductivity:

$$\text{Re}[\sigma_{\eta\eta}] = \frac{1}{\omega a_0^3} \frac{1}{(2\pi)^3} \int_S d\vec{k} \sum_{E_j(\vec{k})<\mu, E_{j'}(\vec{k})>\mu} \frac{2\Gamma |(ea_0/\hbar) 2\sin k_\eta B'_\eta(\vec{k})_{jj'}|^2}{[\hbar\omega - E_{j'}(\vec{k}) + E_j(\vec{k})]^2 + (2\Gamma)^2}, \tag{30}$$

where S is the first Brillouin zone for the paramagnetic state. The explicit expressions of $B'_\eta(\vec{k})$ for $H^{300\ \text{K}}_{\text{nonint}}$ and $H^{300\ \text{K,HF}}_{\text{tot}}$ are given in Appendices B and C, respectively. Γ may be estimated from the root-mean-square fluctuation in the hopping amplitude; we find

$$\Gamma \approx t_0 \sqrt{\langle \cos^2(\theta/2)\rangle - \langle \cos(\theta/2)\rangle^2} \approx \frac{t_0}{3\sqrt{2}}. \tag{31}$$

E. Determination of the parameters

We first determine t_0, λ, and $J_H S_c$ by fitting the band structure of $H^{0\ \text{K}}_{\text{nonint}}$ to the LDA band structure,[9] and determine the Coulomb interaction by comparing the Jahn-Teller peak position in the optical conductivity of $H^{300\ \text{K,HF}}_{\text{tot}}$ with experimental data. From crystallographic studies in Ref. 7, we obtain $\overline{w} = 0.488$ Å and $\overline{v} = 0.174$ Å at $T=0$ K. For our fitting, we use the LDA band calculation for the JT distorted $LaMnO_3$ by Satpathy *et al.*[9] at high symmetry points in re-

ciprocal space, $(\pi,0,0)$, $(0,0,0)$, $(\pi/2,\pi/2,\pi/2)$, and $(\pi,0,\pi/2)$. The standard deviation is ≈ 0.2 eV, and the maximal error of 0.4 eV occurs at $(\pi/2,\pi/2,\pi/2)$ for the lower JT level of the upper Hund state, $E_{5,6}$. The determined parameter values are $t_0=0.622$ eV, $\lambda=1.38$ eV/Å , and $2J_{\mathrm{H}}S_{\mathrm{c}}=2.47$ eV. The fitted band structure is shown in Fig. 1. The dots represent the energy levels from the LDA band calculation in Ref. 9, which we used to fit our model. These parameters fit the LDA band calculations for the JT distorted and buckled actual $LaMnO_3$ structure published by Satpathy *et al.*[8] with a similar size of error. The above values of t_0 and $J_{\mathrm{H}}S_{\mathrm{c}}$ are similar to the values obtained by Mryasov *et al.*[16] from an LDA calculation for the ideal cubic structure.

The parameter λ may be independently determined by fitting the observed lattice distortions[7] to a simple model of localized electrons that are Jahn-Teller-coupled to a harmonic lattice as explained in Ref. 17. This reference shows that the amplitudes of the observed distortions fix the parameter $\lambda/(K_1a_0)$, where K_1 is the force constant for compression of the Mn-O bond, and a_0 is the average Mn-O distance. After correcting a factor of 2 error in Eq. (10) of Ref. 17, we obtain

$$\frac{\lambda}{K_1a_0}=\sqrt{\left(e^z\frac{1+2K_2/K_1}{2}\right)^2+\left(\frac{2u_s^x}{\sqrt{3}a_0}\right)^2}, \qquad (32)$$

where K_2 is an extra parameter related to the elastic modulus $c_{11}-c_{12}$, e^η $(\eta=x,y,z)$ is the uniform strain, and u_s^η is the staggered oxygen displacement. From the results of Ellemans *et al.*,[7] $e^z=-0.0288$, $u_s^x=0.141$ Å , and $a_0=4.034$ Å. For $0\leqslant K_2/K_1\leqslant 1.0$, we obtain $0.0428\leqslant\lambda/(K_1a_0)\leqslant 0.0591$. K_1 is estimated from the frequency of the highest-lying bond-stretching mode measured in this material by Jung and Noh.[18] The measured bond-stretching mode has a peak at 70.3 meV. From the relation $(\hbar\omega)^2=2K_1(m_{\mathrm{Mn}}^{-1}+m_{\mathrm{O}}^{-1})$, we obtain $K_1=7.36$ eV/Å^2. Therefore, we obtain λ between 1.27 eV/Å and 1.76 eV/Å, which includes the value obtained above. We can, in fact, determine the lower bound of K_2/K_1 from the structural transition temperature as explained in Ref. 17. In Ref. 17, the mean-field estimation of the structural phase transition temperature was found to be $T_{\mathrm{s}}^{\mathrm{MF}}=3\lambda^2K_2/[2K_1(K_1+2K_2)]$. By comparing $T_{\mathrm{s}}^{\mathrm{MF}}$ with the observed structural transition temperature 750 K (=65 meV) and considering that mean-field theory overestimates transition temperature, we obtain

$$\frac{3}{2}\frac{\lambda^2K_2}{K_1(K_1+2K_2)}>65 \text{ meV}. \qquad (33)$$

Combining Eqs. (32) and (33), we can determine the range of K_2/K_1. The determined range is $K_2/K_1>0.26$, and gives $\lambda>1.36$ eV/Å, which is remarkably close to the value obtained by the band fitting.

We will use the optical conductivity to estimate the size of the Coulomb interaction. First, as the simplest case, we consider the case where $U_{(\alpha,a),(\beta,b)}=U$, independent of (α,a) and (β,b). Roughly speaking, the presence of the Coulomb interaction U shifts all peaks of the optical conductivity upward by $\approx U$, since in the ground state of $LaMnO_3$ every site has one electron, and any excitation puts two electrons at the same site. Therefore, we use the values of t_0, λ, and $J_{\mathrm{H}}S_{\mathrm{c}}$ obtained from the band fitting, and determine the value of U by calculating optical conductivity and fitting the peak position to the experimental peak position. We use the JT peak for this fitting, since this peak is most prominent. We obtain $U=1.6$ eV. Details of the optical conductivity results will be explained in the next section.

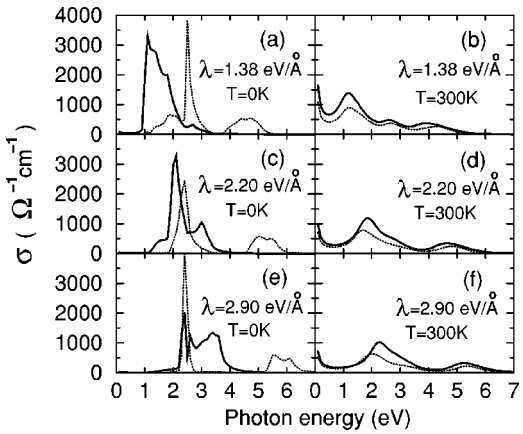

FIG. 2. Optical conductivities σ_{xx} (solid lines) and σ_{zz} (dotted lines) for $t_0=0.622$ eV and $2J_{\mathrm{H}}S_{\mathrm{c}}=2.47$ eV without the Coulomb repulsion term (i.e., $U=0$).

III. RESULTS OF THE CALCULATION

A. At $T=0$ K without the Coulomb interaction term

Figures 2(a), 2(c), and 2(e) show the $T=0$ K optical conductivities σ_{xx} and σ_{zz} calculated for three values of the coupling constant λ with t_0 and $J_{\mathrm{H}}S_{\mathrm{c}}$ predicted by the band theory and $\overline{v}$ and $\overline{w}$ from the crystallographic data. Figure 2(a) shows σ_{xx} and σ_{zz} for the case $2\lambda\sqrt{\overline{v}^2+\overline{w}^2}<2J_{\mathrm{H}}S_{\mathrm{c}}$. For σ_{xx} (solid line), we see a large peak at the Jahn-Teller splitting, corresponding to motion within one plane. Note the jump in absorption at the gap edge—a characteristic two-dimensional feature. A weak feature is also visible at $2J_{\mathrm{H}}S_{\mathrm{c}}$; this corresponds to the electron trajectories that overlap from one plane to the next. An extremely weak feature is also visible at the sum of the Jahn-Teller and Hund's splittings (JT+Hund). For σ_{zz} (dotted line), we see a very weak feature at the Jahn-Teller energy, corresponding to a small amplitude for an electron to tunnel through an intervening plane and land on a ''correctly oriented'' core spin, a large peak at the Hund's energy, and another peak at the sum of the Hund's and Jahn-Teller splitting energies. The sharp peak at the Hund's energy in σ_{zz} originates from the essentially parallel bands seen in Fig. 1 between $(\pi/2,\pi/2,\pi/2)$ and $(\pi,0,\pi/2)$. In the LSDA band calculation in Ref. 9, these two bands are not exactly parallel: The mean splitting varies by $\sim\pm 0.17$ eV, which should induce a comparable broadening of $\epsilon=0.17$ eV. The effect of this broadening is further discussed in Sec. V. Figure 2(c) shows the case of comparable Hund's and Jahn-Teller couplings. We see that the structure becomes more complicated as the features overlap, and the band structure becomes less two-dimensional. The low-energy shoulder starting from 1 eV originates from the transition between the opposite spin directions. Finally, Fig. 2(e) shows the case of a Jahn-Teller coupling greater than the

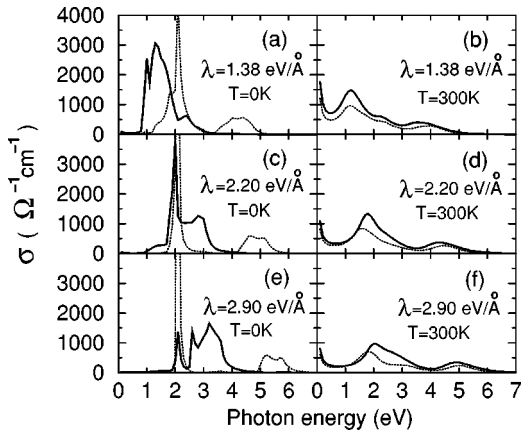

FIG. 3. Optical conductivities σ_{xx} (solid lines) and σ_{zz} (dotted lines) for $t_0=0.622$ eV and $2J_HS_c=2.10$ eV without the Coulomb repulsion term (i.e., $U=0$).

Hund's coupling. In this case the Hund's features appear strongly for both σ_{xx} and σ_{zz}, whereas the Jahn-Teller feature is almost absent in σ_{zz}. Figures 3(a), 3(c), and 3(e) show the results for a lower value of J_HS_c, which show similar features as Figs. 2(a), 2(c), and 2(e). The results for a larger value of J_HS_c are shown in Figs. 4(a), 4(c), and 4(e).

We have also studied the change of optical conductivity caused by the change of the ordered orbital state. The orbital ordering angle θ defined in Sec. II is related to the lattice distortion $\bar{v}$ and $\bar{w}$ by

$$\cos 2\theta = -\frac{\bar{v}}{\sqrt{\bar{v}^2+\bar{w}^2}}. \tag{34}$$

For the observed $\bar{v}$ and $\bar{w}$ at $T=0$ K, we obtain $\theta\approx 54°$. We have varied the ratio between $\bar{v}$ and $\bar{w}$ without changing the JT splitting $2\lambda\sqrt{\bar{v}^2+\bar{w}^2}$. The results are shown in Fig. 5. When $\theta=30°$, the orbital ordering is x^2-z^2/y^2-z^2 type, and when $\theta=60°$, $3x^2-r^2/3y^2-r^2$ type. When $\theta=45°$, the orbital state is between these two configurations. As the ordered orbital state changes from x^2-z^2/y^2-z^2 to $3x^2-r^2/3y^2-r^2$, the total spectral weight of σ_{zz} has substantially decreased. If θ is further varied toward $\theta=90°$, which corresponds to the nonstaggered x^2-y^2 type orbital ordering, then the z-direction conductivity becomes even smaller. For σ_{xx}, as θ decreases, the spectral weight has moved close to the lower edge without appreciable changes in the total spectral weight.

B. At $T_N \ll T \ll 800$ K without the Coulomb interaction term

The general features of σ_{xx} and σ_{zz} at $T \gg T_N$ are these: Because we have random spin directions along both x and z directions, both σ_{xx} and σ_{zz} show the JT, Hund, and JT +Hund peaks. Due to the anisotropy of the lattice distortion, we still expect anisotropy in the peak intensity. The broadening due to the random spin directions means that the peaks become smoother than the $T=0$ K case.

Optical conductivities calculated for the room temperature are shown in Figs. 2(b), 2(d), and 2(f). For these calculations, we use the same λ, t_0, and J_HS_c as in Figs. 2(a), 2(c), and 2(e), but we use the room-temperature lattice parameters, which differ slightly from the 0 K lattice parameters. We obtain $\bar{w}=0.417$ Å and $\bar{v}=0.155$ Å from Ref. 7. As expected, the peaks are substantially broadened and indeed in Figs. 2(d) and 2(f) only two peaks are visible. The upturn of the optical conductivity at around zero frequency is an artifact of our choice of the energy-independent level broadening Γ. Figures 3(b), 3(d), 3(f), 4(b), 4(d), and 4(f) show similar results, obtained for the parameters used in Figs. 3(a), 3(c), 3(e), 4(a), 4(c), and 4(e), respectively.

We show in Table II the variation of the spectral weight with temperature and parameter values. The results obtained from Eq. (27) and from direct integration of σ [as in Eq. (26)] are in agreement. The temperature dependence comes from the familiar double-exchange-driven correlation between spin order and spin-dependent hopping amplitude. It is complicated at small J_HS_c by competition between accessibility of different orbitals and spin-dependent hopping, but at larger J_HS_c the expected decrease in K_{av}, as T is changed from 0 to 300 K, is always seen. Table II shows that at $T=0$ K, K_{xx} sensitively decreases as λ increases, but is insensitive to J_HS_c, while K_{zz} decreases as λ or J_HS_c increases, which can be understood from the spin and lattice configuration at $T=0$ K. On the other hand, at $T=300$ K, both K_{xx} and K_{zz} have moderate dependence on both λ and

TABLE II. Total spectral weights for $t_0=0.622$ eV without the Coulomb interaction term (i.e., $U=0$), expressed in terms of K_x, K_z, and K_{av} for $T=0$ K and 300 K.

$2J_HS_c$ (eV)	λ (eV/Å)	$K_x^{0\ K}$ (eV)	$K_z^{0\ K}$ (eV)	$K_{av}^{0\ K}$ (eV)	$K_x^{300\ K}$ (eV)	$K_z^{300\ K}$ (eV)	$K_{av}^{300\ K}$ (eV)
2.10	1.38	0.295	0.242	0.277	0.290	0.211	0.264
2.10	2.20	0.236	0.226	0.206	0.248	0.179	0.225
2.10	2.90	0.196	0.184	0.192	0.219	0.155	0.198
2.47	1.38	0.294	0.217	0.268	0.277	0.199	0.251
2.47	2.20	0.235	0.185	0.218	0.236	0.167	0.213
2.47	2.90	0.195	0.165	0.185	0.207	0.144	0.186
4.00	1.38	0.289	0.149	0.242	0.249	0.159	0.219
4.00	2.20	0.239	0.129	0.202	0.209	0.139	0.186
4.00	2.90	0.194	0.110	0.166	0.179	0.109	0.156

$J_H S_c$. The spectral weight of each peak depends sensitively on temperature. Particularly, when the Jahn-Teller splitting is much less than the Hund's splitting [as in Figs. 2(a) and 2(b)], it is possible to identify the lowest-energy feature at both 0 K and 300 K as arising from the transitions between the parallel-spin but different Jahn-Teller states, and to determine the spectral weight in this feature. When we define

$$K_{\eta,\mathrm{JT}}=\frac{2\hbar^2 a_0}{\pi e^2}\int_{\mathrm{JT\ peak}} d\omega\sigma_{\eta\eta}(\omega), \tag{35}$$

we find $K_{x,\mathrm{JT}}^{0\ \mathrm{K}}=0.271$ eV, $K_{x,\mathrm{JT}}^{300\ \mathrm{K}}=0.151$ eV for Figs. 2(a) and 2(b), whose ratio is between 1/2 and 2/3, as predicted in Ref. 3. The extra $T=0$ K JT spectral weight is pulled down from the higher-energy peaks as the spin disorder is decreased. It is also noteworthy that the peak shape is more asymmetric at $T=0$ K than at $T=300$ K, due to the two-dimensional character.

C. With the Coulomb interaction term

The experimental results of Ref. 19 show the lowest-energy peak at 2.5 eV, which we interpret as the JT peak. This peak position is about 1.3 eV higher than our results obtained without the Coulomb interaction term. We believe that the difference comes from the Coulomb interaction. By fitting the calculated peak position to the experimental peak position we estimate the size of the Coulomb interaction. We obtain $U=1.6$ eV. This value of U is close to the difference of the experimental peak position and the calculated peak position for the $U=0$ case. The room-temperature results are shown in Figs. 6(b) and 6(d). As we increase the value of U, the peak position shifts upwards by $\approx U$, and the peak intensity decreases. With this determined value of U, we calculate the $T=0$ K results shown in Figs. 6(a) and 6(c). It shows that as T is changed from 300 K to 0 K, the anisotropy is enhanced and the spectral weight of the JT peak in σ_{av} is increased approximately twice.

We briefly mention the more general case in which $U_{(\alpha,a),(\beta,b)}$ depends on the indices, i.e., the Coulomb repulsion depends on precisely which spin and orbital states are occupied. In the no-hopping case, the energy levels on each site are $-\lambda'_{\Uparrow}\sqrt{\overline{v^2}+\overline{w^2}}$, $\lambda'_{\Uparrow}\sqrt{\overline{v^2}+\overline{w^2}}$, $2J'_H S_c-\lambda'_{\Downarrow}\sqrt{\overline{v^2}+\overline{w^2}}$, and $2J'_H S_c+\lambda'_{\Downarrow}\sqrt{\overline{v^2}+\overline{w^2}}$. Even though the finite hopping gives dispersion to these energy levels, the peak positions are close to the energy differences between different levels. Therefore, the JT peak position is close to $2\lambda'_{\Uparrow}\sqrt{\overline{v^2}+\overline{w^2}}$, the Hund peak position is close to $2J'_H S_c+(\lambda'_{\Uparrow}-\lambda'_{\Downarrow})\sqrt{\overline{v^2}+\overline{w^2}}$, and the JT+Hund peak position is close to $2J'_H S_c+(\lambda'_{\Uparrow}+\lambda'_{\Downarrow})\sqrt{\overline{v^2}+\overline{w^2}}$. To see the effects of the different types of the Coulomb interaction, we use different values of $\lambda'_{\Downarrow}$, $J'_H S_c$ for the same value of $\lambda'_{\Uparrow}$, and calculate the optical conductivities. We found that the JT peak position and spectral weight do not change very much. Therefore, even if we use a more general Coulomb interaction with $U_{(\alpha,a),(\beta,b)}$ dependent on the indices, as far as we fix the JT peak position by fixing $\lambda'_{\Uparrow}$, its spectral weight does not change very much.

For the above model, we also calculate the variation of the level occupancies as a function of U. The results for the lowest-lying orbital $\langle\hat{n}_{\Uparrow,-}\rangle$ are shown in Fig. 7 for $T=0$ K and $T=300$ K, which shows that as U increases, the e_g elec-

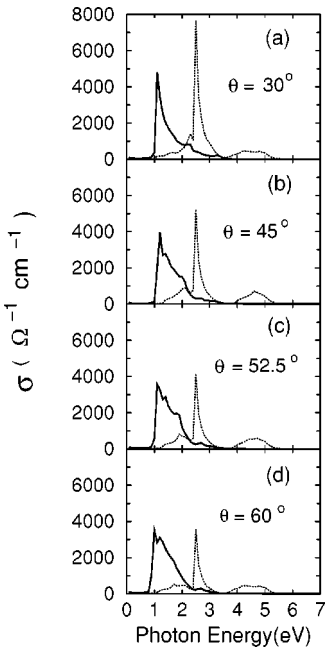

FIG. 5. Optical conductivities σ_{xx} (solid lines) and σ_{zz} (dotted lines) for $t_0=0.622$ eV, $2J_H S_c=2.47$ eV, $\lambda=1.38$ eV/Å, and $U=0$ with different orbital ordering angle θ.

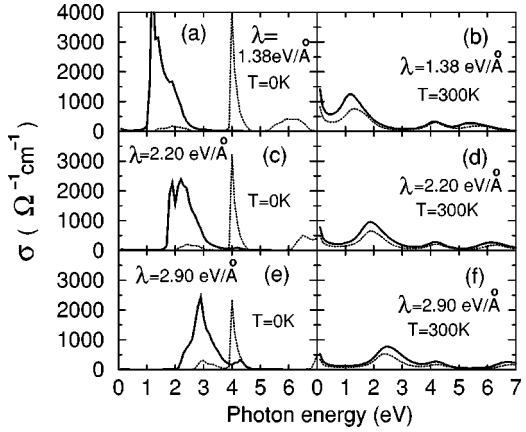

FIG. 4. Optical conductivities σ_{xx} (solid lines) and σ_{zz} (dotted lines) for $t_0=0.622$ eV and $2J_H S_c=4.0$ eV without the Coulomb repulsion term (i.e., $U=0$).

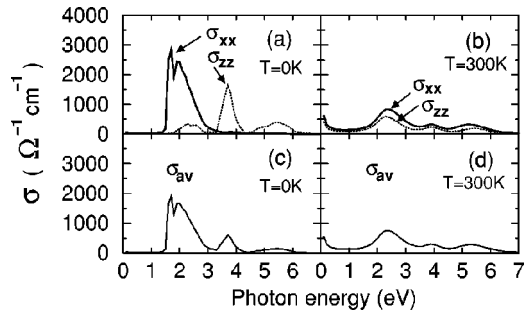

FIG. 6. Optical conductivities for $t_0=0.622$ eV, $2J_H S_c=2.47$ eV, $\lambda=1.38$ eV/Å, and $U=1.59$ eV.

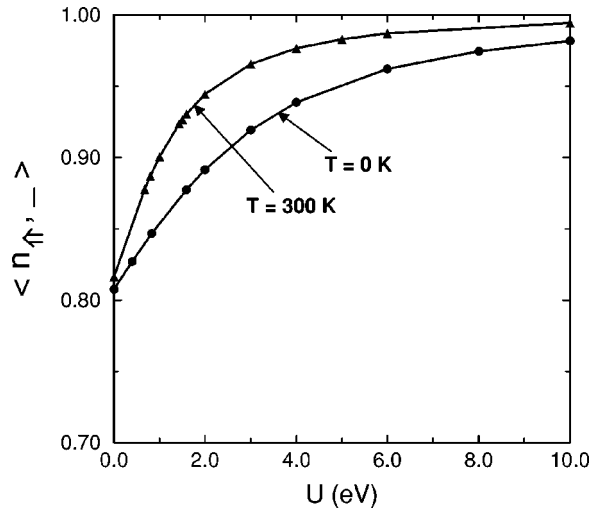

FIG. 7. Occupancies of the lowest-lying orbital versus U for $t_0=0.622$ eV, $2J_HS_c=2.47$ eV, and $\lambda=1.38$ eV/Å at $T=0$ K and 300 K. $\langle \hat{n}_{\Uparrow -}\rangle$ for $T=300$ K is smaller than that for $T=0$ K due to the reduced kinetic energy in the paramagnetic state as mentioned in Sec. III B. For example, $K_{\rm av}^{0\ \rm K}=0.268$ eV, $K_{\rm av}^{300\ \rm K}=0.251$ eV for $U=0$ eV, $K_{\rm av}^{0\ \rm K}=0.207$ eV, $K_{\rm av}^{300\ \rm K}=0.149$ eV for $U=2$ eV, and $K_{\rm av}^{0\ \rm K}=0.087$ eV, $K_{\rm av}^{300\ \rm K}=0.050$ eV for $U=10$ eV.

trons are more likely to have spins parallel to the core spins and stay in the ground state of the local lattice distortion. The curves, however, show that the value of U required to fit the data of Ref. 19 does not change the ground-state occupancy much.

IV. COMPARISON WITH EXPERIMENTS

We now compare our results to data. This comparison is preliminary because the available data disagree. Optical conductivity for polycrystalline $LaMnO_3$ was measured at room temperature by Jung *et al.*[20] Because the crystal directions are random in polycrystalline samples, the observed quantity is $\sigma_{\rm av}=2\sigma_{xx}/3+\sigma_{zz}/3$, provided that the crystallite size is large. We have also plotted our calculated $\sigma_{\rm av}$ for $H_{\rm nonint}^{300\ \rm K}$ in Fig. 8. Figure 8(a) shows the results for the parameter values determined from the band fitting. The data in Ref. 20 exhibit

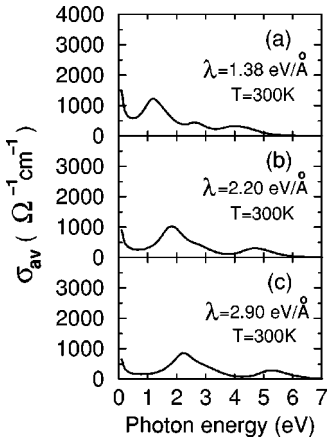

FIG. 8. Average optical conductivities $\sigma_{\rm av}$ for $t_0=0.622$ eV and $2J_HS_c=2.47$ eV at $T=300$ K without the Coulomb repulsion term (i.e., $U=0$).

two main structures; a lower peak centered at 1.9 eV with maximum intensity 420 $\Omega^{-1}\,\mathrm{cm}^{-1}$ and integrated intensity corresponding to $K_{\rm av,JT}=2K_{x,\rm JT}/3+K_{z,\rm JT}/3\approx 0.115$ eV, and a peak centered at around 4.5 eV with a much larger intensity. The authors of Ref. 20 attribute the 4.5 eV feature to the e_g–O 2p transitions beyond the scope of our model and assign the peak at 1.9 eV to the JT-split e_g-e_g transitions within the parallel-spin manifold. In this interpretation, the transitions to the reversed spin states are obscured by the Mn-O transitions. Recently, room-temperature optical reflectivity spectra using a cleaved single-crystal surface of $La_{1-x}Sr_xMnO_3$ have been measured by Takenaka *et al.*[19] Although it is referred to as a single crystal, we believe that the sample of $LaMnO_3$ is microtwinned. In Ref. 19, the Jahn-Teller peak appears at around 2.5 eV with maximum intensity $\approx 600\ \Omega^{-1}\,\mathrm{cm}^{-1}$ and width ≈ 1.5 eV corresponding to $K_{\rm av,JT}\approx 0.141$ eV, and the Mn-O peak appears at 5 eV with maximum intensity $\approx 2800\ \Omega^{-1}\,\mathrm{cm}^{-1}$. Similar results were obtained by Okimoto *et al.*[2] The results of Takenaka *et al.* show a weak shoulder at 1.9 eV that our model cannot explain. The two different experiments therefore disagree by 30% in peak position and 20% in spectral weight. Further, the experiment reporting the lower gap value has a lower spectral weight, a trend opposite to that found in any reasonable model. We therefore regard the experimental situation as uncertain.

From Fig. 8(a), it is plain that if the Jahn-Teller interaction were the only important one, the observed lattice distortions would lead to a peak in $\sigma_{\rm av}$ at 1.2 eV with maximum intensity $\approx 1200\ \Omega^{-1}\,\mathrm{cm}^{-1}$, width ≈ 1.0 eV, and $K_{\rm av,JT}\approx 0.223$ eV. The maximum intensity or spectral weight is much larger than the observed values in either experiment, and the peak position is lower. From Fig. 8(c), we see that the data of Ref. 19 may be approximately modeled by use of a stronger electron lattice coupling or a nonzero Coulomb interaction, which moves the peak to higher energy and reduces its spectral weight. For the data in Ref. 20, one cannot simultaneously fit the peak amplitude and the peak position as can be seen from Fig. 3(b): Choosing interaction parameters to fit the peak position leads to an amplitude that is too large. The combination of peak energy and amplitude could only be explained if the actual hopping were significantly smaller than the band-theory value (say $t_0\approx 0.4$ eV rather than 0.6 eV).

Further optical data would be very desirable (especially measurements at lower T). For the present we assume the data of Ref. 19 are correct, and consider their interpretation in more detail. We believe that the combination of the band calculation and the estimates from the crystallographic data adequately fix the magnitude of the Jahn-Teller splitting. We therefore believe that the differences between the data of Ref. 19 and Fig. 8(a) are mainly due to the Coulomb interaction whose effects we have studied in Sec. III C. For $U=1.6$ eV, the calculated maximum peak intensity is 730 $\Omega^{-1}\,\mathrm{cm}^{-1}$, the width is 1.2 eV, and $K_{\rm av,JT}^{300\ \rm K}\approx 0.145$ eV, which is close to the observed spectral weight in Ref. 19. Because our choice of the parameters reproduces both the peak position and the spectral weight, we believe our model is in reasonable agreement with the experiment at $T=300$ K. We emphasize, however, that the true test of our results is

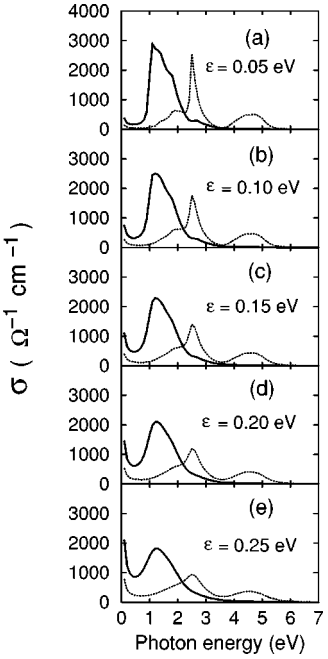

FIG. 9. Optical conductivities σ_{xx} (solid lines) and σ_{zz} (dotted lines) for $t_0=0.622$ eV, $2J_HS_c=2.47$ eV, $\lambda=1.38$ eV/Å, and $U=0$ with different broadening ϵ.

the predicted strong temperature dependence, which has not yet been observed.

V. UNCERTAINTIES

In this section we present a detailed discussion of possible errors in our results. There are two motivations: First, tight-binding-based many-body calculations are widely used to understand experimental data, so a discussion of their correctness is needed. Second, $\sigma(\omega,T=0\ \mathrm{K})$ was calculated[5,6,21] for $LaMnO_3$ using band-theory-based methods involving explicit construction of wave functions and evaluation of matrix elements. These works disagree with each other, most notably in the spectral weight in the peak we have identified as the JT feature: The spectral weight in the Jahn-Teller peak at 2 eV shown in Fig. 1 of Ref. 21 is twice that in Fig. 8 of Ref. 5. Our average spectral weight calculated for $U=0$ and $\lambda=1.38$ eV/Å, is close to the results in Ref. 21 and is about twice as large as that found in Ref. 5. The difference is particularly troubling, because the tight-binding Peierls phase formalism omits further-neighbor hopping and on-site transitions between *s* and *p* symmetry orbitals, and therefore might be expected to underestimate the spectral weight, not to overestimate.

We compare our results in more detail to those of Ref. 6, which disagree with ours in two respects. First, the form is different: The sharp peaks we find are absent in their calculation. We suspect that the difference is due in part to the 0.01 Ry $\approx$0.14 eV level broadening employed in Ref. 6 and in part to the oversimplicity of our tight-binding model. Figure 9 shows the effects of introducing an artificial broadening ϵ into our calculation; the result is to be compared with Fig. 2(a). This figure shows that as the artificial broadening is increased, the peaks diminish in amplitude and become more symmetrical (although there is always more asymmetry in our calculation than in Ref. 6). Regarding the oversimplicity of our model, our nearest-neighbor tight-binding fit predicts that certain bands are parallel, while in the actual band structure a certain curvature is present due to small second-neighbor hoppings, as noted in Sec. III A. This effect will give an additional broadening $\approx$0.2 eV to the Hund's peak in σ_{zz}. Therefore, the total broadening for the Hund's peak in σ_{zz} in Ref. 6 relative to our result will be $\epsilon\approx$0.3 eV, which explains the difference in line shape, which is not of fundamental importance for this paper.

A far more serious discrepancy is the difference in spectral weight. The area under the lowest conductivity peak in Ref. 6 is about a factor of 4 smaller than in our calculation, and as noted one expects the tight-binding model to underestimate the spectral weight. This difference seems not to be caused by trivial errors in our calculation. In Sec. III B, direct integration of σ [Eq. (26)] and the *f*-sum rule expression [Eq. (27)] were shown to agree. We may verify our results also in a different way. According to the Hellman-Feynman theorem, $K=K_{xx}+K_{yy}+K_{zz}$ can be found from the ground-state energy E_0/N_{Mn} by

$$K=-t_0\frac{d(E_0/N_{\mathrm{Mn}})}{dt_0}, \tag{36}$$

where t_0 is the hopping parameter defined in Sec. II B 2. At $T=0$ K, we have calculated E_0/N_{Mn} as the sum of energies of the filled bands,

$$\frac{E_0}{N_{\mathrm{Mn}}}=\frac{2}{(2\pi)^3}\int_R d\vec{k}[E_1(\vec{k})+E_2(\vec{k})] \tag{37}$$

and evaluated *K* using Eq. (36). The result obtained in this way is in agreement with the results in Table II.

We next examine the size of the possible error due to the following two approximations we have made: First, we have assumed that the hopping between Mn ions, which originates from the Mn-O hopping, can be effectively represented without explicit consideration of the O band. Second, we have used the tight-binding approximation.

To study the effects of the Mn-O hybridization on the conductivity in the dominantly Mn bands, we consider a simple model of a one-dimensional Mn-O chain along the *x* direction. Each unit cell contains one Mn ion at position $R_i^{\mathrm{Mn}}=n_ia_0$ with a *d* orbital represented by $d_i^\dagger$, and one oxygen ion at position $R_i^{\mathrm{O}}=(n_i+1/2)a_0$ with a *p* orbital represented by $p_i^\dagger$. We consider a Mn-O hopping of magnitude $t_{\mathrm{Mn\text{-}O}}$ and choose the sign to reflect the symmetry of the O *p* orbital (the sign can be removed by change of *k* space origin). In addition, to model the Jahn-Teller distortion, we consider alternating periodic potential Δ on the Mn site. We represent the energy of the *d* level relative to the *p* level by *V*. For simplicity we assume spinless electrons. This can be represented by the following Hamiltonian:

$$H=-\frac{t_{\mathrm{Mn\text{-}O}}}{2}\sum_i\ (d_i^\dagger p_i-p_i^\dagger d_{i+1}-d_{i+1}^\dagger p_i+p_i^\dagger d_i+\mathrm{H.c.})$$
$$+\sum_i\frac{\Delta}{2}(-1)^i d_i^\dagger d_i-Vp_i^\dagger p_i. \tag{38}$$

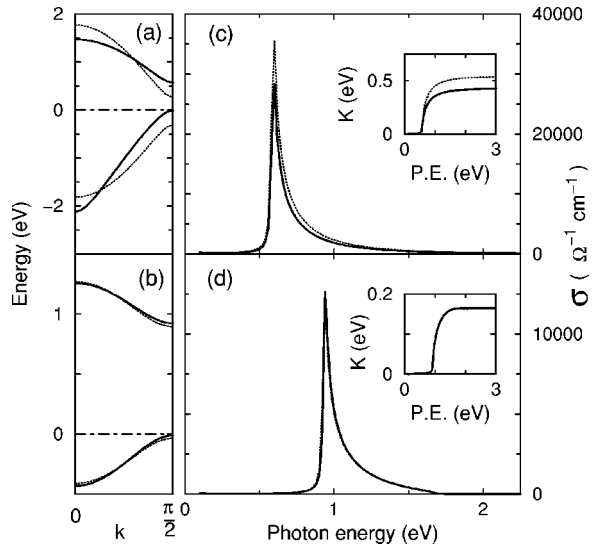

FIG. 10. Mn *d*-band structures [(a), (b)] and optical conductivities [(c), (d)] of the Mn-O chain in the model explicitly considering the O *p* level (solid lines) and in the best-fit effective Mn-Mn chain model (dotted lines). The used parameter values are $t_{\text{Mn-O}}=2.0$ eV, $\Delta=1.0$ eV, $V=1.0$ eV, $t_{\text{eff}}=0.88$ eV, and $\Delta_{\text{eff}}=0.59$ eV for (a) and (c), and $t_{\text{Mn-O}}=2.0$ eV, $\Delta=1.0$ eV, $V=10$ eV, $t_{\text{eff}}=0.35$ eV, and $\Delta_{\text{eff}}=0.93$ eV for (b) and (d). The insets show the integrated spectral weight represented in terms of kinetic energy (K) versus photon energy (P.E.).

We obtain the exact band structure and optical conductivity for the above Hamiltonian, and compare these to the band structure and conductivity obtained from the nearest-neighbor tight-binding fit to the two uppermost (Mn-dominant) bands. The difference turns out to be small. The effective tight-binding Hamiltonian is

$$H_{\text{eff}}=-\frac{t_{\text{eff}}}{2}\sum_i\,(d_i^\dagger d_{i+1}+d_i^\dagger d_{i-1}+\text{H.c.})$$

$$+\sum_i\,\frac{\Delta_{\text{eff}}}{2}(-1)^i d_i^\dagger d_i\,. \tag{39}$$

By transforming into k space, we can find the band structure for H and H_{eff}. The band structure of H_{eff} is simply given by

$$E=\pm\sqrt{4t_{\text{eff}}^2\cos^2 k+\frac{\Delta_{\text{eff}}^2}{4}}. \tag{40}$$

For given $t_{\text{Mn-O}}$, Δ, and V, we can fit the band structure of H_{eff} to that of H to determine t_{eff} and Δ_{eff}.

For $t_{\text{Mn-O}}=2.0$ eV and $\Delta=1.0$ eV, we study $V=1.0$ eV and 10 eV cases. The obtained *d* bands are shown in Figs. 10(a) and 10(b) ($V=1.0$ eV and 10 eV, respectively) as solid lines, along with the best Mn-band tight-binding fit as dotted lines. The fitted parameter values are $t_{\text{eff}}=0.88$ eV, $\Delta_{\text{eff}}=0.59$ eV for $V=1.0$ eV, and $t_{\text{eff}}=0.35$ eV, $\Delta_{\text{eff}}=0.93$ eV for $V=10$ eV. It shows that when $V=1.0$ eV, the fitting has an error of 10% of the *d*-band width (comparable to the error in the fits used in Secs. II–IV), but when $V=10$ eV, the fitting has negligible error. For these two cases, we assume half filling, and calculate optical conductivities which are shown in Figs. 10(c) and 10(d). The insets show the integrated spectral weight, $K(\hbar\omega)=(2\hbar^2 a_0/\pi e^2)\int_0^{\hbar\omega}\sigma(\omega)d\omega$. In this calculation, we assumed the Mn-Mn distance is $a_0=4.034$ Å, and the cross-sectional area perpendicular to the direction of the chain is a_0^2. For $V=10$ eV, the two calculations give almost identical results. For $V=1.0$ eV, the tight-binding fit has about 25% larger spectral weight. We therefore expect our Mn-only approximation yields errors $\approx 25\%$.

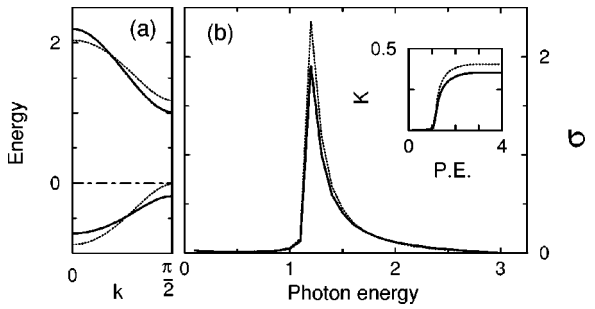

FIG. 11. Band structures [(a)] and optical conductivities [(b)] for the exact Kronig-Penney model [Eq. (41)] with $V_1=-4$, $V_2=-5$ (solid lines) and for the best tight-binding fit with $t_{\text{eff}}=1.33$, $\Delta_{\text{eff}}=0.6$ (dotted lines). The inset shows the integrated spectral weight represented in terms of kinetic energy (K) versus photon energy (P.E.).

Next, to estimate the error of the tight-binding approximation (i.e., of the Peierls approximation to the optical matrix elements), we consider the following Kronig-Penney (KP) model:

$$\hat{H}=-\frac{1}{2}\frac{d^2}{dx^2}+\sum_{n=-\infty}^{\infty}\left[\frac{V_1}{2}\delta(x-2n-1)+\frac{V_2}{2}\delta(x-2n)\right], \tag{41}$$

where V_1, $V_2<0$, $\hbar=m_e=e=1$, and spinless electrons are assumed for simplicity. Once the values of V_1 and V_2 are given, we can find the eigenstates $\psi_k(x)$, the band structure, and the optical conductivity, and compare these to the Peierls approximation. The band structure has two bands; at $n=1/2$, one is filled and the other is empty. Therefore, we can calculate the optical conductivity via

$$\sigma=\frac{1}{\omega}\frac{1}{2\pi}\int_{-\pi/2}^{\pi/2}\frac{|\langle 2,k|d/dx|1,k\rangle|^2\epsilon}{[\omega-E_2(k)+E_1(k)]^2+\epsilon^2}, \tag{42}$$

where 1 and 2 are the band indices. For $V_1=-4$, $V_2=-5$, we calculate the exact band structure, shown as solid lines in Fig. 11(a) along with the best tight-binding fit from Eq. (39) ($t_{\text{eff}}=1.33$, $\Delta_{\text{eff}}=0.6$) shown as solid lines. It shows that the error is about 7% of the total bandwidth. Figure 11(b) shows the calculated optical conductivities for the exact KP model and the tight-binding fit. The spectral weight of the tight-binding fit is about 20% larger than that of the exact result, as shown in the inset.

For $LaMnO_3$, our band fitting has an error of about 0.2 eV, which corresponds to about 5% of the total Mn $e_g\uparrow$ bandwidth. So, we expect our approximation to have a similar size error in spectral weight as the two cases considered above. Thus, we expect that our calculated optical conductivity may have overestimated spectral weight by about 20%. Therefore, we believe that within this error our approximations are valid.

The relation between the kinetic energy and the optical spectral weight follows from the two assumptions of gauge invariance and reasonably localized *d*-electron wave functions. The success of the tight-binding fit confirms this localized character. A tight-binding parametrization of the band structure has been used to study $\sigma(\omega)$ in other correlated electron contexts,[14,22] and seems to work well for high-T_c superconductors. The apparent discrepancy between the LDA and the tight-binding methods and between the different LDA calculations found for manganites is thus an important issue for future research.

VI. CONCLUSION

We have calculated the optical conductivity of $LaMnO_3$ and have shown that the available data are consistent with the band-theory estimate for the hopping parameter t_0 and the lattice-distortion-induced e_g-level splitting. Our main prediction that the functional form and magnitude of σ change as T is decreased below T_N is contained in Fig. 6. The experimental determination of the Hund's coupling as well as the final validation of our model must await definitive measurements of the magnitude and temperature dependence of $\sigma(\omega)$.

In conclusion, we comment on the implications of our results. First, we note that the estimate of the electron-lattice coupling derived from band theory is in good agreement with that derived directly from the crystallographic data as shown in Sec. II E, and the room-temperature spectral weights suggest that the band-theory estimate of the hopping parameter is not far off, implying the relevance of a bandlike description. Second, we observe that the electron-lattice interaction by itself does not account for the magnitude of the gap or the spectral weight in the absorption spectrum. A Coulomb interaction $U \approx 1.6$ eV is also required. This value puts $LaMnO_3$ in the weak-intermediate coupling range: The Coulomb interaction is approximately 40% of the full bandwidth $6t_0 \approx 3.6$ eV. In the simple one-band Hubbard model, a Coulomb interaction of this size (relative to the bandwidth) does not significantly affect properties (such as optical spectral weights) at reasonable dopings of order 0.2 or larger. The effects of this moderate Coulomb coupling on properties of models of doped manganites deserve further attention. Many authors have argued on the basis of photoemission data[23] that the Coulomb repulsion is large (5–10 eV); however, as noted by the experimentalists themselves, because the manganites are charge-transfer rather than the Mott-Hubbard materials (as are the high-T_c superconductors) the U measured in photoemission is not directly relevant to the low- ($\hbar\omega < 4$ eV) energy physics of interest here.

Our data analysis focuses on robust features (peak positions and spectral weights) and is insensitive (at the 20% level) to the approximations we made. Uncertainties in the tight-binding parametrization of the band structure lead to an error ≈ 0.2 eV in peak position, which is not important here; the consistency of the peak position and spectral weight leads us to believe that the band-theory estimates of t_0 are reasonably accurate. Uncertainties in the estimates of the electron-phonon coupling λ could change our estimated Coulomb repulsion by around 0.2 eV, which is also insignificant. We note, however, that we have not included any excitonic effects arising from the first-neighbor interactions such as those proposed by Maekawa and co-workers.[24] At $T=0$ K, the two-dimensional character and general flatness of the bands suggest that these might be important and interesting to look for.

The crucial prediction of the present model is the dramatic change in the optical absorption with temperature. This change is a robust feature of the model, and comes from a dramatic shift in spectral weight caused by the ferromagnetic spin ordering, along with a very nearly two-dimensional character of the bands at $T \to 0$ K caused by the between-plane antiferromagnetism. Early data[2] reported only a weak temperature dependence of the optical absorption; if these data are reproduced, then our fundamental picture of the manganites based on e_g electron with electron-lattice and electron-electron interactions must be modified.

Finally, we note that a troubling discrepancy with LDA band-theory calculations of the optical conductivity exists. Further work is needed to find the origin of the difference.

Note added in proof: Orbital angle θ in Sec. III A is defined by $|0\rangle = \cos\theta |3z^2 r^2\rangle + \sin\theta |y^2 - x^2\rangle$.

ACKNOWLEDGMENTS

We thank L. Benedict, H. Drew, S. Louie, O. Mryasov, and M. Quijada for helpful discussions. This work was supported by Grant No. NSF-DMR-9705182 and the University of Maryland MRSEC.

APPENDIX A: HAMILTONIAN IN k SPACE AT $T=0$ K

Without considering the Coulomb repulsion, the total Hamiltonian at $T=0$ K is given by the following expression:

$$H_{\text{nonint}}^{0\text{ K}} = \sum_{\alpha=\uparrow,\downarrow,\vec{k}\in R} d_{\alpha,\vec{k}}^{\dagger} H_{\text{nonint},\alpha}^{0\text{ K}}(\vec{k}) d_{\alpha,\vec{k}}, \tag{A1}$$

where

$$d_{\alpha,\vec{k}}^{\dagger} = (d_{1,\vec{k},\alpha}^{\dagger}, d_{2,\vec{k},\alpha}^{\dagger}, d_{1,\vec{k}+(\pi,\pi,0),\alpha}^{\dagger}, d_{2,\vec{k}+(\pi,\pi,0),\alpha}^{\dagger}, d_{1,\vec{k}+(0,0,\pi),\alpha}^{\dagger}, d_{2,\vec{k}+(0,0,\pi),\alpha}^{\dagger}, d_{1,\vec{k}+(\pi,\pi,\pi),\alpha}^{\dagger}, d_{2,\vec{k}+(\pi,\pi,\pi),\alpha}^{\dagger}), \tag{A2}$$

$$H_{\text{nonint},\alpha}^{0\text{ K}}(\vec{k}) = \begin{pmatrix} M_1+G+V & W & G_\alpha & 0 \\ W & M_2+G+V & 0 & G_\alpha \\ G_\alpha & 0 & M_3+G+V & W \\ 0 & G_\alpha & W & M_4+G+V \end{pmatrix}, \tag{A3}$$

$$M_1=\begin{pmatrix} -\frac{t_0}{2}(\cos k_x+\cos k_y+4\cos k_z) & \frac{\sqrt{3}t_0}{2}(\cos k_x-\cos k_y) \\ \frac{\sqrt{3}t_0}{2}(\cos k_x-\cos k_y) & -\frac{3t_0}{2}(\cos k_x+\cos k_y) \end{pmatrix}, \tag{A4}$$

$$M_2=\begin{pmatrix} \frac{t_0}{2}(\cos k_x+\cos k_y-4\cos k_z) & -\frac{\sqrt{3}t_0}{2}(\cos k_x-\cos k_y) \\ -\frac{\sqrt{3}t_0}{2}(\cos k_x-\cos k_y) & \frac{3t_0}{2}(\cos k_x+\cos k_y) \end{pmatrix}, \tag{A5}$$

$$M_3=\begin{pmatrix} -\frac{t_0}{2}(\cos k_x+\cos k_y-4\cos k_z) & \frac{\sqrt{3}t_0}{2}(\cos k_x-\cos k_y) \\ \frac{\sqrt{3}t_0}{2}(\cos k_x-\cos k_y) & -\frac{3t_0}{2}(\cos k_x+\cos k_y) \end{pmatrix}, \tag{A6}$$

$$M_4=\begin{pmatrix} \frac{t_0}{2}(\cos k_x+\cos k_y+4\cos k_z) & -\frac{\sqrt{3}t_0}{2}(\cos k_x-\cos k_y) \\ -\frac{\sqrt{3}t_0}{2}(\cos k_x-\cos k_y) & \frac{3t_0}{2}(\cos k_x+\cos k_y) \end{pmatrix}, \tag{A7}$$

$$G=\begin{pmatrix} J_{\mathrm{H}}S_{\mathrm{c}} & 0 \\ 0 & J_{\mathrm{H}}S_{\mathrm{c}} \end{pmatrix}, \tag{A8}$$

$$G_{\uparrow}=-G, \tag{A9}$$

$$G_{\downarrow}=G, \tag{A10}$$

$$V=\begin{pmatrix} \lambda\overline{v} & 0 \\ 0 & -\lambda\overline{v} \end{pmatrix}, \tag{A11}$$

$$W=\begin{pmatrix} 0 & -\lambda\overline{w} \\ -\lambda\overline{w} & 0 \end{pmatrix}, \tag{A12}$$

$$R=\{\vec{k}\,||k_x|+|k_y|<\pi \text{ and } |k_z|<\pi/2\}. \tag{A13}$$

$B_\eta(\vec{k})$, which is used to calculate optical conductivity, is given by

$$B_\eta(\vec{k})=D(\vec{k})^{\dagger}T_\eta D(\vec{k}), \tag{A14}$$

$$T_x=\begin{pmatrix} t_x & 0 & 0 & 0 \\ 0 & -t_x & 0 & 0 \\ 0 & 0 & t_x & 0 \\ 0 & 0 & 0 & -t_x \end{pmatrix}, \tag{A15}$$

$$T_y=\begin{pmatrix} t_y & 0 & 0 & 0 \\ 0 & -t_y & 0 & 0 \\ 0 & 0 & t_y & 0 \\ 0 & 0 & 0 & -t_y \end{pmatrix}, \tag{A16}$$

$$T_z=\begin{pmatrix} t_z & 0 & 0 & 0 \\ 0 & t_z & 0 & 0 \\ 0 & 0 & -t_z & 0 \\ 0 & 0 & 0 & -t_z \end{pmatrix}, \tag{A17}$$

where $D(\vec{k})$ is the matrix diagonalizing $H^{0\ \mathrm{K}}_{\mathrm{nonint}}(\vec{k})$ given above. t_x, t_y, and t_z are the 2×2 matrices defined in Sec. II B 2.

APPENDIX B: HAMILTONIAN IN k SPACE AT $T=300$ K

Without considering the Coulomb repulsion, the effective total Hamiltonian at $T=300$ K is given by the following expression:

$$H^{300\ \mathrm{K}}_{\mathrm{nonint}}=\sum_{\vec{k}\in S} d^{\dagger}_{\vec{k}}H^{300\ \mathrm{K}}_{\mathrm{nonint}}(\vec{k})d_{\vec{k}}, \tag{B1}$$

where

$$d^{\dagger}_{\vec{k}}=(d^{\dagger}_{1,\vec{k},\Uparrow},d^{\dagger}_{2,\vec{k},\Uparrow},d^{\dagger}_{1,\vec{k}+(\pi,\pi,0),\Uparrow},d^{\dagger}_{2,\vec{k}+(\pi,\pi,0),\Uparrow},d^{\dagger}_{1,\vec{k},\Downarrow},d^{\dagger}_{2,\vec{k},\Downarrow},d^{\dagger}_{1,\vec{k}+(\pi,\pi,0),\Downarrow},d^{\dagger}_{2,\vec{k}+(\pi,\pi,0),\Downarrow}), \tag{B2}$$

$$H^{300\ \mathrm{K}}_{\mathrm{nonint}}(\vec{k})=\begin{pmatrix} \frac{2}{3}M_1+V & W & \frac{2}{3}M_1 & 0 \\ W & \frac{2}{3}M_2+V & 0 & \frac{2}{3}M_2 \\ \frac{2}{3}M_1 & 0 & \frac{2}{3}M_1+V+2G & W \\ 0 & \frac{2}{3}M_2 & W & \frac{2}{3}M_2+V+2G \end{pmatrix}, \tag{B3}$$

$$S=\{\vec{k}\,|\,|k_x|+|k_y|<\pi \ \text{ and } \ |k_z|<\pi\}. \tag{B4}$$

M_1, M_2, V, W, and G are defined in Appendix A. $B'_\eta(\vec{k})$, which is used to calculate optical conductivity, is given by

$$B'_\eta(\vec{k})=D'(\vec{k})^\dagger T'_\eta D'(\vec{k}), \tag{B5}$$

$$T'_x=\frac{2}{3}\begin{pmatrix} t_x & 0 & t_x & 0 \\ 0 & -t_x & 0 & -t_x \\ t_x & 0 & t_x & 0 \\ 0 & -t_x & 0 & -t_x \end{pmatrix}, \tag{B6}$$

$$T'_y=\frac{2}{3}\begin{pmatrix} t_y & 0 & t_y & 0 \\ 0 & -t_y & 0 & -t_y \\ t_y & 0 & t_y & 0 \\ 0 & -t_y & 0 & -t_y \end{pmatrix}, \tag{B7}$$

$$T'_z=\frac{2}{3}\begin{pmatrix} t_z & 0 & t_z & 0 \\ 0 & t_z & 0 & t_z \\ t_z & 0 & t_z & 0 \\ 0 & t_z & 0 & t_z \end{pmatrix}, \tag{B8}$$

and $D'(\vec{k})$ is the matrix diagonalizing $H^{300\ \mathrm{K}}_{\mathrm{nonint}}(\vec{k})$.

APPENDIX C: HAMILTONIAN IN *k* SPACE WITH THE COULOMB INTERACTION

We define λ'_{av} and $\delta\lambda'$ by

$$\lambda'_{\Uparrow}=\lambda'_{av}+\delta\lambda', \tag{C1}$$

$$\lambda'_{\Downarrow}=\lambda'_{av}-\delta\lambda'. \tag{C2}$$

At $T=0$ K, the total Hartree-Fock Hamiltonian with the Coulomb interaction,

$$H^{0\ \mathrm{K,HF}}_{\mathrm{tot}}=\sum_{\alpha=\uparrow,\downarrow,\vec{k}\in R} d^\dagger_{\alpha,\vec{k}} H^{0\ \mathrm{K,HF}}_{\mathrm{tot},\alpha}(\vec{k}) d_{\alpha,\vec{k}}, \tag{C3}$$

consists of two terms: One has the same form as $H^{0\ \mathrm{K}}_{\mathrm{nonint}}$ in Appendix A with $J_{\mathrm{H}}S_{\mathrm{c}}\rightarrow J'_{\mathrm{H}}S_{\mathrm{c}}$ and $\lambda\rightarrow\lambda'_{\mathrm{av}}$, while the other additional term is

$$H^{0\ \mathrm{K,HF}}_{\mathrm{add}}=\sum_{\alpha=\uparrow,\downarrow,\vec{k}\in R} d^\dagger_{\alpha,\vec{k}} H^{0\ \mathrm{K,HF}}_{\mathrm{add},\alpha}(\vec{k}) d_{\alpha,\vec{k}}, \tag{C4}$$

where

$$H^{0\ \mathrm{K,HF}}_{\mathrm{add},\alpha}(\vec{k})=\begin{pmatrix} 0 & 0 & \delta\overline{V}_\alpha & \delta\overline{W}_\alpha \\ 0 & 0 & \delta\overline{W}_\alpha & \delta\overline{V}_\alpha \\ \delta\overline{V}_\alpha & \delta\overline{W}_\alpha & 0 & 0 \\ \delta\overline{W}_\alpha & \delta\overline{V}_\alpha & 0 & 0 \end{pmatrix}, \tag{C5}$$

$$\delta\overline{V}_\alpha=\begin{pmatrix} \delta\lambda'_\alpha\overline{v} & 0 \\ 0 & -\delta\lambda'_\alpha\overline{v} \end{pmatrix}, \tag{C6}$$

$$\delta\overline{W}_\alpha=\begin{pmatrix} 0 & -\delta\lambda'_\alpha\overline{w} \\ -\delta\lambda'_\alpha\overline{w} & 0 \end{pmatrix}, \tag{C7}$$

$$\delta\lambda'_{\uparrow}=\delta\lambda', \tag{C8}$$

$$\delta\lambda'_{\downarrow}=-\delta\lambda'. \tag{C9}$$

Similarly, for $T=300$ K the total Hartree-Fock Hamiltonian with the Coulomb interaction,

$$H^{300\ \mathrm{K,HF}}_{\mathrm{tot}}=\sum_{\vec{k}\in S} d^\dagger_{\vec{k}} H^{300\ \mathrm{K,HF}}_{\mathrm{tot}}(\vec{k}) d_{\vec{k}}, \tag{C10}$$

consists of two terms: One has the same form as $H^{300\ \mathrm{K}}_{\mathrm{nonint}}$ in Appendix B with $J_{\mathrm{H}}S_{\mathrm{c}}\rightarrow J'_{\mathrm{H}}S_{\mathrm{c}}$ and $\lambda\rightarrow\lambda'_{av}$, while the other additional term is

$$H^{300\ \mathrm{K,HF}}_{\mathrm{add}}=\sum_{\vec{k}\in S} d^\dagger_{\vec{k}} H^{300\ \mathrm{K,HF}}_{\mathrm{add}}(\vec{k}) d_{\vec{k}}, \tag{C11}$$

where

$$H^{300\ \mathrm{K,HF}}_{\mathrm{add}}(\vec{k})=\begin{pmatrix} \delta\overline{V} & \delta\overline{W} & 0 & 0 \\ \delta\overline{W} & \delta\overline{V} & 0 & 0 \\ 0 & 0 & -\delta\overline{V} & -\delta\overline{W} \\ 0 & 0 & -\delta\overline{W} & -\delta\overline{V} \end{pmatrix}. \tag{C12}$$

$$\delta\overline{V}=\begin{pmatrix} \delta\lambda'\overline{v} & 0 \\ 0 & -\delta\lambda'\overline{v} \end{pmatrix}, \tag{C13}$$

$$\delta\overline{W}=\begin{pmatrix} 0 & -\delta\lambda'\overline{w} \\ -\delta\lambda'\overline{w} & 0 \end{pmatrix}. \tag{C14}$$

With these Hamiltonians for given $U_{(\alpha,a),(\beta,b)}$, we can repeatedly calculate $\langle \hat{n}_{\beta,b} \rangle$ until its value converges. At $T=0$ K, $\langle \hat{n}_{\alpha,a} \rangle$ is given by the following expression:

$$\langle \hat{n}_{\alpha,a} \rangle = \frac{1}{(2\pi)^3} \int_R d\vec{k} \sum_{j=1,2} [P_\uparrow(\vec{k})^\dagger Q_{\uparrow\alpha a} P_\uparrow(\vec{k})]_{jj} + [P_\downarrow(\vec{k})^\dagger Q_{\downarrow\alpha a} P_\downarrow(\vec{k})]_{jj}, \tag{C15}$$

where

$$Q_{\uparrow\Uparrow,\pm} = Q_{\downarrow\Downarrow,\pm} = Q_{1\pm}, \tag{C16}$$

$$Q_{\downarrow\Uparrow,\pm} = Q_{\uparrow\Downarrow,\pm} = Q_{2\pm}, \tag{C17}$$

$$Q_{1\pm} = \begin{pmatrix} A_\pm & B_\pm & A_\pm & B_\pm \\ B_\pm & A_\pm & B_\pm & A_\pm \\ A_\pm & B_\pm & A_\pm & B_\pm \\ B_\pm & A_\pm & B_\pm & A_\pm \end{pmatrix}, \tag{C18}$$

$$Q_{2\pm} = \begin{pmatrix} A_\pm & B_\pm & -A_\pm & -B_\pm \\ B_\pm & A_\pm & -B_\pm & -A_\pm \\ -A_\pm & -B_\pm & A_\pm & B_\pm \\ -B_\pm & -A_\pm & B_\pm & A_\pm \end{pmatrix}, \tag{C19}$$

$$A_\pm = \begin{pmatrix} \alpha_\pm^2/2 & 0 \\ 0 & \beta_\pm^2/2 \end{pmatrix}, \tag{C20}$$

$$B_\pm = \begin{pmatrix} 0 & \alpha_\pm\beta_\pm/2 \\ \alpha_\pm\beta_\pm/2 & 0 \end{pmatrix}, \tag{C21}$$

$$\alpha_\pm = \frac{\overline{w}}{\sqrt{2(\overline{v^2}+\overline{w^2}) \mp 2\overline{v}\sqrt{\overline{v^2}+\overline{w^2}}}}, \tag{C22}$$

$$\beta_\pm = \frac{\overline{v} \mp \sqrt{\overline{v^2}+\overline{w^2}}}{\sqrt{2(\overline{v^2}+\overline{w^2}) \mp 2\overline{v}\sqrt{\overline{v^2}+\overline{w^2}}}}, \tag{C23}$$

and $P_\alpha(\vec{k})$ is the matrix diagonalizing $H_{tot,\alpha}^{0\ \mathrm{K,HF}}(\vec{k})$.

At $T=300$ K,

$$\langle \hat{n}_{\alpha,a} \rangle = \frac{1}{(2\pi)^3} \int_S d\vec{k} \sum_{j=1,2} [P'(\vec{k})^\dagger Q'_{\alpha a} P'(\vec{k})]_{jj}, \tag{C24}$$

where

$$Q'_{\Uparrow\pm} = 2\begin{pmatrix} A_\pm & B_\pm & 0 & 0 \\ B_\pm & A_\pm & 0 & 0 \\ 0 & 0 & 0 & 0 \\ 0 & 0 & 0 & 0 \end{pmatrix}, \tag{C25}$$

$$Q'_{\Downarrow\pm} = 2\begin{pmatrix} 0 & 0 & 0 & 0 \\ 0 & 0 & 0 & 0 \\ 0 & 0 & A_\pm & B_\pm \\ 0 & 0 & B_\pm & A_\pm \end{pmatrix}, \tag{C26}$$

and $P'(\vec{k})$ is the matrix diagonalizing $H_{\mathrm{tot}}^{300\ \mathrm{K,HF}}(\vec{k})$.

$B_\eta(\vec{k})$ and $B'_\eta(\vec{k})$ for the optical conductivity with the Coulomb interaction term are obtained by using $P(\vec{k})$ and $P'(\vec{k})$ instead of $D(\vec{k})$ and $D'(\vec{k})$, respectively, in Eqs. (A14) and (B5).

*On leave from the Department of Physics and Astronomy, The Johns Hopkins University, Baltimore, Maryland 21218.

[1] See, e.g., the articles in Philos. Trans. R. Soc. London, Ser. A **356**, pp. 1469–1712 (1998), special issue on *Understanding and Utilizing Colossal Magnetoresistance Materials*, edited by M. Blamire, L. F. Cohen, D. M. Edwards, and J. L. Macmanus-Driscoll.

[2] Y. Okimoto, T. Katsufuji, T. Ishikawa, T. Arima, and Y. Tokura, Phys. Rev. B **55**, 4206 (1997).

[3] M. Quijada, J. Černe, J. R. Simpson, H. D. Drew, K. H. Ahn, A. J. Millis, R. Shreekala, R. Ramesh, M. Rajeswari, and T. Venkatesan, Phys. Rev. B **58**, 16 093 (1998).

[4] T. Saitoh, A. E. Bocquet, T. Mizokawa, H. Namatame, A. Fujimori, M. Abbate, Y. Takeda, and M. Takano, Phys. Rev. B **51**, 13 942 (1995).

[5] I. Solovyev, N. Hamada, and K. Terakura, Phys. Rev. B **53**, 7158 (1996).

[6] K. Terakura, I. V. Solovyev, and H. Sawada, in *Colossal Magnetoresistive Oxides*, edited by Y. Tokura (Gordon and Breach, Tokyo, 1999).

[7] J. B. A. A. Ellemans, B. van Laar, K. R. van der Veen, and B. O. Loopstra, J. Solid State Chem. **3**, 238 (1971).

[8] S. Satpathy, Z. S. Popovic, and F. R. Vukajlovic, Phys. Rev. Lett. **76**, 960 (1996).

[9] S. Satpathy, Z. S. Popovic, and F. R. Vukajlovic, J. Appl. Phys. **79**, 4555 (1996).

[10] W. E. Pickett and D. J. Singh, Phys. Rev. B **53**, 1146 (1996).

[11] M. S. Hybertsen and M. Schlüter, Phys. Rev. B **39**, 9028 (1989).

[12] P. W. Anderson, *The Theory of Superconductivity in the High-T_c Cuprates* (Princeton University Press, Princeton, NJ, 1997).

[13] C. A. Stafford, Ph.D. thesis, Princeton University, 1992.

[14] E. Dagotto, Rev. Mod. Phys. **66**, 763 (1994).

[15] A. J. Millis and S. Coppersmith, Phys. Rev. B **42**, 10 807 (1990).

[16] O. Mryasov, S. Ilani, and A. Freeman (unpublished).

[17] A. J. Millis, Phys. Rev. B **53**, 8434 (1996).

[18] J. H. Jung and T. W. Noh (private communication).

[19] K. Takenaka, K. Iida, Y. Sawaki, S. Sugai, Y. Moritomo, and A. Nakamura, J. Phys. Soc. Jpn. **68**, 1828 (1999).

[20] J. H. Jung, K. H. Kim, D. J. Eom, T. W. Noh, E. J. Choi, J. Yu, Y. S. Kwon, and Y. Chung, Phys. Rev. B **55**, 15 489 (1997).

[21] S. Bouarab, A. Vega, and M. A. Khan, Phys. Rev. B **54**, 11 271 (1996).

[22] D. Baeriswyl, J. Carmelo, and A. Luther, Phys. Rev. B **33**, 7247 (1986).

[23] T. Saitoh, A. Sekiyama, K. Kobayashi, T. Mizokawa, A. Fujimori, D. D. Sarma, Y. Takeda, and M. Takano, Phys. Rev. B **56**, 8836 (1997).

[24] S. Maekawa, J. Magn. Magn. Mater. **177**, 850 (1998); W. Koshibae, Y. Kawamura, I.-L. Inoue, and S. Maekawa, J. Phys. Soc. Jpn. **66**, 2985 (1997).